

# Preserving SOC for enhancement of spin-to-charge conversion efficiency via Cu intercalation in MoS<sub>2</sub>/CoFeB heterostructures

Abhisek Mishra,<sup>1</sup> Pritam Das,<sup>2</sup> Rupalipriyadarsini Chhatoi,<sup>1</sup> Soubhagya Dash,<sup>1</sup> Shubhransu Sahoo,<sup>1</sup> Kshitij Singh Rathore,<sup>1</sup> Pil-Ryung Cha,<sup>2</sup> Seung-Cheol Lee,<sup>3</sup> Satadeep Bhattacharjee,<sup>4,\*</sup> and Subhankar Bedanta<sup>1,5,†</sup>

<sup>1</sup>Laboratory for Nanomagnetism and Magnetic Materials, School of Physical Sciences, National Institute of Science Education and Research (NISER), An OCC of Homi Bhabha National Institute (HBNI), Jatni 752050, India.

<sup>2</sup>School of Advanced Material Engineering, Kookmin University, Seoul 02707, Republic of Korea

<sup>3</sup>Korea Institute of Science and Technology, Seoul, Republic of Korea

<sup>4</sup>Indo-Korea Science and Technology Center (IKST), Bangalore, India

<sup>5</sup>Center for Interdisciplinary Sciences (CIS), National Institute of Science Education and Research (NISER), An OCC of Homi Bhabha National Institute (HBNI), Jatni 752050, India.

(Dated: November 28, 2024)

Transition metal dichalcogenides (TMDs) are a novel type of quantum materials that could be used in spintronics, optoelectronics, valleytronics and opto-valleytronics. The phenomena of spin-to-charge conversion at the interface between sputtered magnetic materials and transition metal dichalcogenides have gained attention for designing fast and ultra-low power consumption devices that are applicable for spintronic-based applications. Here, we report a remarkable enhancement of spin-to-charge conversion efficiency in MoS<sub>2</sub>/CoFeB heterostructures via Cu intercalation. In this context, magneto-optic Kerr effect-based microscopy reveals the absence of substantial domain modification due to Cu which indicates that Cu successfully detaches MoS<sub>2</sub> from CoFeB. This shows that Cu interlayer is protecting the spin orbit coupling (SOC) of MoS<sub>2</sub> from exchange interaction with CoFeB, since the proximity with local magnetization can alter the electronic structure and hence the SOC. Further, via first-principles calculations, it is found that notable improvements in spin Berry curvature and spin Hall conductivity occur via the Cu intercalation which in turn increases the spin Hall angle. We have shown here that one can modify interfaces of ferromagnet and transition metal dichalcogenides-based heterostructures to achieve higher efficiencies of spin-to-charge conversion across them for extended functionalities and its relevance in spin orbit torque-based applications.

Keywords: Transition metal dichalcogenides, Anisotropy, MOKE, FMR, Spin orbit coupling, Thin films, DFT

## INTRODUCTION

The exploration and use of spin currents in information processing devices have become a major focus of scientific research due to their potential to reduce power consumption and enhance operational speed. Achieving high-density spin currents in materials having high spin orbit coupling (HS) strength is essential for the progress of spintronic applications [1–3]. Among the numerous mechanisms explored, spin pumping has demonstrated a significant potential [4]. This technique involves generating substantial spin current densities in materials having high SOC placed adjacent to a ferromagnet (FM) or ferrimagnet (FiM) with a precessing magnetization. Notably, spin pumping is effective in heterostructures comprising HS materials of metallic, insulating and semiconducting in nature, addressing the challenge of impedance mismatch and enhancing the feasibility of spintronic devices. Traditionally, the spin Hall effect (SHE) and its Onsager reciprocal, the inverse spin Hall effect (ISHE), were the primary recognized mechanisms for bidirectional conversion of spin and charge currents [5, 6]. These effects are driven by electron scattering processes in three-dimensional materials with substantial SOC, such as

heavy metals like Pt, Pd, W and Ta etc, antiferromagnetic materials like IrMn, Mn<sub>2</sub>Au, Mn<sub>3</sub>Ga, Mn<sub>3</sub>Sn etc, and topological insulators like Bi<sub>2</sub>Se<sub>3</sub>, Bi<sub>2</sub>Te<sub>3</sub> etc [7–12]. In this context, recent advancements have recognized transition metal dichalcogenides (TMDs) as promising quantum materials for enhanced spin and charge conversion efficiency [13]. The high SOC in TMDs enables effective interconversion of charge current and spin current through the SHE and ISHE. Among TMDs, molybdenum disulfide (MoS<sub>2</sub>) is notable for its stability, robustness and distinctive electronic properties, which exhibit significant variations depending on thickness and mechanical strain [14–17]. In MoS<sub>2</sub>/FM heterostructure, due to the interface the global anisotropy has been found to be enhanced substantially [18, 19]. In addition to these, MoS<sub>2</sub> has been demonstrated to show significant spin to charge conversion voltage and hence a large conversion efficiency in numerous FM/MoS<sub>2</sub> heterostructures [20–23]. Further, the efficiency of spin to charge conversion in these FM/HS systems has been shown to be enhanced by manipulating the interface via intercalators such as Ag, Cu, Ti etc [24–26]. These interlayers behave as potential barriers between the FM and HS layers, which preserve their SOC by eliminating the proximity-induced magnetic ef-

fects in spin-to-charge conversion experiments. By taking the help of these low SOC spacer layers, one can tune the spin-dependent interfacial resistivity as well as the spin injection. In this context, Cu has been proven to be a suitable material owing to its long spin diffusion length ( $\sim 350$  nm) [27], low SOC, and its ability to control the spin transmissivity in spin-based devices.

Here, we report a significant enhancement in the spin Hall angle (SHA) of MoS<sub>2</sub> via Cu intercalation in MoS<sub>2</sub>/CoFeB films. Domain imaging via magneto-optic Kerr microscopy indicates that the Cu intercalation decouples MoS<sub>2</sub> from CoFeB which helps in preserving the SOC of MoS<sub>2</sub>. Further, we explain the experimental findings by theoretical calculations based on density functional theory (DFT).

## EXPERIMENTAL DETAILS

A high vacuum multi-deposition chamber (manufactured by Mantis Deposition Ltd., UK) with a base pressure better than  $4 \times 10^{-8}$  mbar was utilized to prepare the thin films of MoS<sub>2</sub>(5 nm)/Cu ( $t_{Cu}$  nm)/CoFeB (9 nm)/AlO<sub>X</sub>(3 nm) with variable Cu thicknesses. MoS<sub>2</sub>, Co<sub>40</sub>Fe<sub>40</sub>B<sub>20</sub> (CoFeB) and AlO<sub>X</sub> films were deposited from commercially available stoichiometric targets. Cu and CoFeB were deposited via dc magnetron sputtering whereas MoS<sub>2</sub> and AlO<sub>X</sub> were deposited by rf sputtering. The samples were grown on a Si (100) substrate with 300 nm thick SiO<sub>2</sub> layer. Samples are named M1, M2, M3, M4, M5, M6, and M7, corresponding to Cu thicknesses ( $t_{Cu}$ ) of 0, 0.65, 2, 3, 5, 7, and 10 nm, respectively. The reference layer CoFeB (9 nm)/AlO<sub>X</sub> (3nm) is named as M0. The magnetization dynamics and ISHE measurements have been performed via ferromagnetic resonance (FMR). Saturation magnetization was measured with a SQUID-based magnetometer (MPMS 3, Quantum Design). The magnetization reversal in all the samples was investigated through magnetic hysteresis loop measurements (see Fig. S7, SI), accompanied by simultaneous domain imaging using a magneto-optic Kerr effect (MOKE) microscope configured in longitudinal geometry. The detailed experimental protocol has been described in the supplementary information (SI).

## RESULTS AND DISCUSSION

The structural information (X-ray reflectivity and Raman spectroscopy) regarding the samples has been mentioned in the SI. The Gilbert damping parameter ( $\alpha$ ) was determined by fitting the resonance field ( $H_{res}$ ) and linewidth ( $\Delta H$ ) data from ferromagnetic resonance spectroscopy, as explained in the SI. The  $\alpha$  ( $\times 10^{-3}$ ) values of the samples M1-M7 are mentioned in Table I, which are higher than that of the reference layer M0 ( $8.2 \pm 0.1$ ).

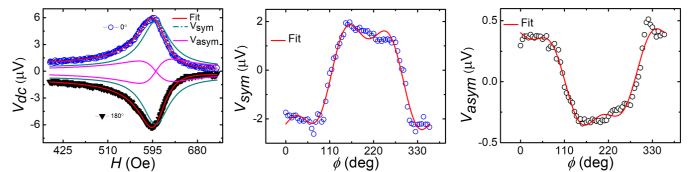


FIG. 1. (a) Measured  $dc$  voltage signals for  $0^\circ$  (open blue symbols) and  $180^\circ$  (solid black triangles) for sample M5 are shown as open circles. The solid red line is the fit to equation (3). The green and magenta lines are the  $V_{sym}$  and  $V_{asym}$  components of the voltage.  $\phi$  dependent (b)  $V_{sym}$  and (c)  $V_{asym}$  for samples M5. Figure (b) is fitted to eqn. (2) while figure (c) is fitted to equation (3).

The elevated  $\alpha$  values in the bilayer and trilayer samples suggest the presence of potential spin pumping. However, the contribution of other effects cannot be excluded. To confirm the presence of spin pumping, we conducted ISHE measurements on these samples. Fig. 1(a) displays the variation in the measured voltage caused by ISHE as a function of the applied field  $H$  for the sample M5 at in-plane angles ( $\phi$ ) 0 and 180 degrees. The symmetric ( $V_{sym}$ ) and antisymmetric ( $V_{asym}$ ) components of the measured voltage signal ( $V_{dc}$ ) were separated by fitting the data to the following Lorentzian equation [28],

$$V_{dc} = V_{sym} \frac{(\Delta H)^2}{(H - H_{res})^2 + (\Delta H)^2} + V_{asym} \frac{2\Delta H(H - H_{res})}{(H - H_{res})^2 + (\Delta H)^2} \quad (1)$$

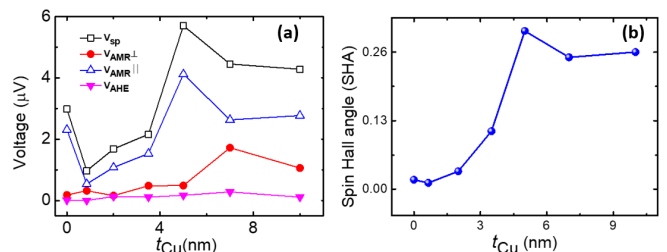


FIG. 2. (a) The voltage contributions due to spin pumping and other spin rectification effects as a function of  $t_{Cu}$ .  $V_{sp}$  shows a dominating contribution over other rectification effects in all the samples. (b) Variation of  $\theta_{SHA}$  as a function of  $t_{Cu}$ .

Here,  $\phi$  represents the angle between the direction of the measured voltage and the direction perpendicular to the applied  $H$ . The reversal in the sign of  $V_{dc}$  as  $\phi$  shifts from  $0^\circ$  to  $180^\circ$  clearly indicates the presence of spin pumping in our samples. In ISHE experiments, the voltage signal detected may also reflect contributions from parasitic spin rectification effects (SREs). SREs arise from the generation of a DC voltage in ferromagnetic layers due to the non-linear coupling between the dynamic resistance  $R$ , which depends on the time-varying

magnetic field  $H(t)$ , and the dynamic current  $I(t)$ . Key factors driving SREs include the anomalous Hall effect (AHE) and anisotropic magnetoresistance (AMR). To obtain the contributions due to AHE and AMR, angle-dependent ISHE measurements were conducted. In Fig. 1(b) and (c), the angle-dependent  $V_{sym}$  and  $V_{asym}$  components, respectively, for sample M5 are shown. The plots were fitted using the following equations [28]:

$$V_{sym} = V_{sp} \cos^3(\phi + \phi_0) + V_{AHE} \cos(\theta) \cos(\phi + \phi_0) + V_{sym}^{AMR\perp} \cos 2(\phi + \phi_0) \cos(\phi + \phi_0) + V_{sym}^{AMR\parallel} \sin 2(\phi + \phi_0) \cos(\phi + \phi_0) \quad (2)$$

$$V_{asym} = V_{AHE} \sin(\theta) \cos(\phi + \phi_0) + V_{asym}^{AMR\perp} \cos 2(\phi + \phi_0) \cos(\phi + \phi_0) + V_{asym}^{AMR\parallel} \sin 2(\phi + \phi_0) \cos(\phi + \phi_0) \quad (3)$$

An additional factor  $\phi_0$  has been included to account for the misalignment in sample positioning when defining the  $\phi$  values during measurements. Here,  $\theta$  is the angle between the electric and magnetic fields of the applied microwave which is  $90^\circ$ . Different voltage components, as determined from the angle-dependent ISHE measurements, are listed in Table I.

It has been observed that  $V_{sp}$  dominates over the rectification effects indicating a strong spin pumping phenomenon as shown in Fig. 2(a). The effective spin mixing conductance, which dictates the amount of spin current that can flow through the interface, was determined using the following expression:

$$g_{eff}^{\uparrow\downarrow} = \frac{\Delta\alpha 4\pi M_S t_{CoFeB}}{g\mu_B} \quad (4)$$

where  $\Delta\alpha$ ,  $M_S$ ,  $t_{CoFeB}$ ,  $\mu_B$  and  $g$  represent the difference in  $\alpha$  from the reference CoFeB layer, the saturation magnetization, the thickness of the CoFeB layer, the Bohr magneton, and the Landé g-factor, respectively. The measured  $g_{eff}^{\uparrow\downarrow}$  values for the samples M1-M7 are mentioned in Table-I. The values of  $g_{eff}^{\uparrow\downarrow}$  in the trilayer structure with Cu are higher compared to the bilayer structure without Cu. This indicates that Cu layer promotes efficient spin transfer across the interface. The values of  $M_S$  obtained from SQUID magnetometry for the samples M0-M7 were found to be  $801 \pm 31$ ,  $840 \pm 25$ ,  $790 \pm 36$ ,  $833 \pm 20$ ,  $843 \pm 32$ ,  $820 \pm 34$ ,  $848 \pm 23$  and  $818 \pm 28$  emu/cc, respectively. We evaluated the spin to charge conversion efficiency of the samples, known as the spin Hall angle ( $\theta_{SHA}$ ), using the following expression [29]:

$$\frac{V_{SP}}{R} = w \times \theta_{SHA} \lambda_{SD} \tanh\left(\frac{t_{MoS_2}}{2\lambda_{SD}}\right) J_s \quad (5)$$

where  $J_s$  is given by,

$$J_s \approx \frac{g_{eff}^{\uparrow\downarrow} \gamma^2 \hbar r_f^2 \hbar [4\pi M_S \gamma + \sqrt{(4\pi M_S \gamma)^2 + 16(\pi f)^2}]}{8\pi\alpha^2 [(4\pi M_S \gamma)^2 + 16(\pi f)^2]} \quad (6)$$

Here,  $w$  represents the transmission linewidth of the coplanar waveguide (CPW),  $R$  is the resistance of the samples measured using the four-probe method, and  $\lambda_{SD}$  is the spin diffusion length. In our setup, the  $rf$  field ( $\mu_0 h_{rf}$ ) is 0.5 Oe, and the transmission line width,  $w$  is 200  $\mu\text{m}$ . We have considered the spin diffusion length of 7.83 nm from our previous report [20]. Fig.2 (b) shows the variation of  $\theta_{SHA}$  as a function of  $t_{Cu}$ .  $\theta_{SHA}$  shows the maximum value of  $0.30 \pm 0.01$  at the  $t_{Cu}$  of 5 nm before further decreasing. This value is one order higher than that of MoS<sub>2</sub>/CoFeB bilayer (sample M1) which is  $0.020 \pm 0.003$ .

The initial decrease in the  $\theta_{SHA}$  could be due to the increased roughness for a 0.65 nm thick Cu layer. At this very thin Cu layer, the finite size effect comes into play [30]. This effect arises because, at these small thicknesses, electron scattering at the surfaces and grain boundaries becomes significant, increasing the overall resistivity. The resistance of the samples varies from  $362 \pm 0.45$  to  $26 \pm 0.09$   $\Omega$  from sample M1 to M7 which indicates the shunting effect due to Cu. This further means that the electrons in the Cu layer experience more scattering events at low thickness of Cu, including spin-flip scattering, which disrupts the spin alignment and reduces the efficiency of spin transport. As a result, the spin Hall angle decreases initially. With increasing Cu thickness, the Cu layer starts to act as a good spin transmitter with minimal dissipation and reduced spin flipping, preserving the spin polarization. This leads to an increase in the spin Hall angle. When the thickness of the Cu layer increases to  $\geq 5$  nm, the Cu layer becomes thick enough to support spin accumulation. This accumulation refers to the buildup of spin-polarized electrons at the interfaces, which can occur when the layer is thick enough to allow spins to diffuse without significant spin-flip scattering. This suggests that the spin Hall angle of the Cu interlayer generates a positive voltage response [31], reducing the net spin Hall angle. In the MoS<sub>2</sub>/CoFeB structure, the direct interface may lead to significant spin dissipation and the formation of mixed electronic states that could hinder efficient spin accumulation. Hence, the Cu interlayer helps decouple these effects, providing an additional cleaner pathway for spin currents to reach the MoS<sub>2</sub> layer.

In order to further confirm the decoupling at the MoS<sub>2</sub>/Cu/CoFeB trilayer, we performed magneto-optic Kerr effect-based microscopy. The domain images presented in Fig. 3. (a-e) indicate the isotropic nature of the reference CoFeB layer (M0). These findings suggest that the CoFeB layer exhibits magnetic isotropy in the film plane, a characteristic commonly observed in amor-

TABLE I.  $\alpha$ ,  $g_{eff}^{\uparrow\downarrow}$  and fitted parameters from the in-plane angle dependent ISHE measurements

Sample	$t_{Cu}$ (nm)	$V_{sp}(V)\times 10^{-6}$	$V_{AHE}(V)\times 10^{-6}$	$V_{AMR}^{\perp}(V)\times 10^{-6}$	$V_{AMR}^{\parallel}(V)\times 10^{-6}$	$\alpha(\times 10^{-3})$	$g_{eff}^{\uparrow\downarrow}(\text{nm}^{-2})$
M1	0	$2.98 \pm 0.08$	$0.18 \pm 0.06$	$2.31 \pm 0.08$	$0.012 \pm 0.001$	$11.40 \pm 0.10$	$14.60 \pm 0.02$
M2	0.65	$0.97 \pm 0.02$	$0.32 \pm 0.01$	$0.54 \pm 0.03$	$0.002 \pm 0.001$	$13.60 \pm 0.10$	$24.70 \pm 0.04$
M3	2	$1.68 \pm 0.05$	$0.16 \pm 0.02$	$1.08 \pm 0.06$	$0.13 \pm 0.03$	$13.20 \pm 0.20$	$27.10 \pm 0.03$
M4	3	$2.16 \pm 0.11$	$0.48 \pm 0.04$	$1.53 \pm 0.12$	$0.11 \pm 0.05$	$13.30 \pm 0.10$	$28.30 \pm 0.20$
M5	5	$5.70 \pm 0.12$	$0.49 \pm 0.01$	$3.36 \pm 0.13$	$0.17 \pm 0.06$	$13.01 \pm 0.10$	$26.20 \pm 0.20$
M6	7	$4.45 \pm 0.13$	$1.72 \pm 0.05$	$2.63 \pm 0.13$	$0.28 \pm 0.06$	$12.80 \pm 0.10$	$25.50 \pm 0.30$
M7	10	$4.28 \pm 0.05$	$1.06 \pm 0.04$	$2.77 \pm 0.05$	$0.11 \pm 0.02$	$12.90 \pm 0.20$	$25.27 \pm 0.20$

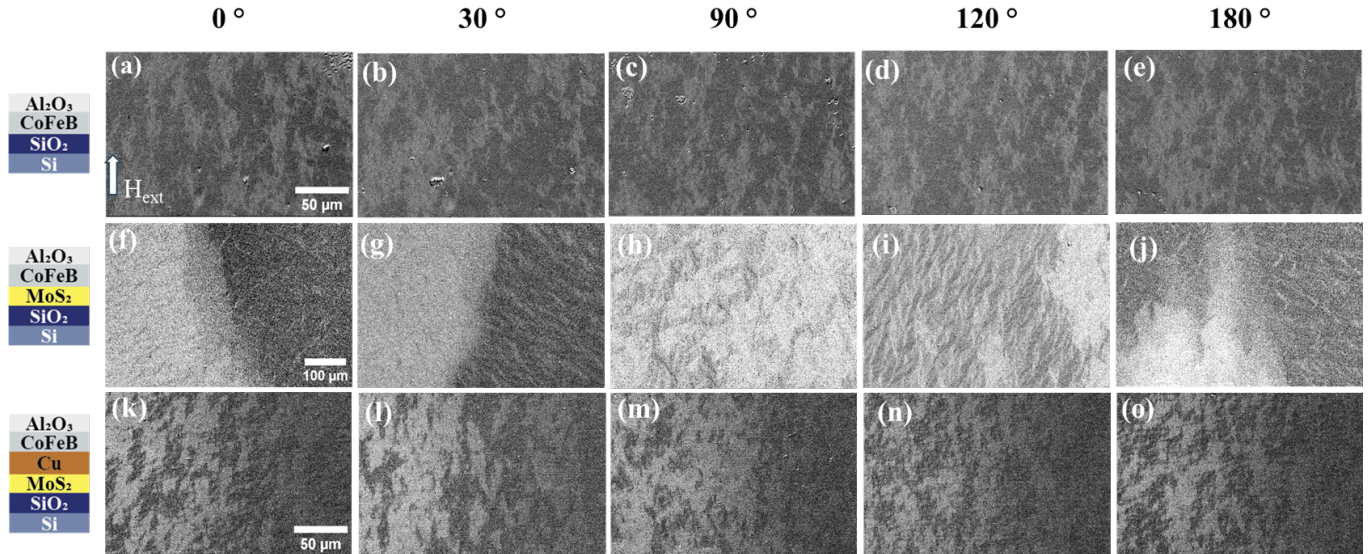


FIG. 3. Domain images captured for samples M0, M1 and M5 at angles  $\phi = 0^\circ, 30^\circ, 90^\circ, 120^\circ$ , and  $180^\circ$  near to coercivity. Magnetic field direction shown in (a) is valid for all the domain images. Scale bars shown in (a), (f) and (k) are valid for (b-e), (g-j) and (l-o), respectively.

phous ferromagnets where magnetocrystalline anisotropy is minimal due to the absence of long-range structural order [32, 33]. In contrast, domain images at  $0^\circ$  and  $180^\circ$  for M1, shown in Fig.3 (f) and (j), reveal large domains, suggesting that magnetization reversal occurs through domain wall nucleation and motion [34]. This implies that  $\text{MoS}_2$  induces substantial anisotropy in the CoFeB layer. Interestingly, when Cu is inserted as a spacer layer between  $\text{MoS}_2$  and CoFeB, the magnetic microstructures of CoFeB are now separated from  $\text{MoS}_2$ , as evidenced by the similar domain images to those of the reference CoFeB layer shown in Fig. 3 (k-o). The domain structures for sample M5, exhibit negligible changes. This indicates that the introduction of the Cu layer effectively prevents any proximity-induced effects at the  $\text{MoS}_2/\text{CoFeB}$  interface that could disrupt spin transport and conversion efficiency.

## THEORETICAL CALCULATIONS

To understand the role of the Cu spacer layer in the spin-pumping we performed first-principles based calculation to estimate the spin Hall angles (SHA) in  $\text{MoS}_2/\text{CoFeB}$  and  $\text{MoS}_2/\text{Cu}/\text{CoFeB}$  systems within the framework of Density Functional Theory (DFT). The detailed methodology of these calculations is mentioned in the SI. The spin Hall angle is given by [35],

$$\theta_{\text{SHA}} = \frac{2e}{\hbar} \frac{\sigma_{xy}^{\text{SHC}}}{\sigma_{xx}} \quad (7)$$

Where  $\sigma_{xy}^{\text{SHC}}$  is the spin Hall conductivity (SHC) and  $\sigma_{xx}$  is the longitudinal charge conductivity. In the present work, we consider the intrinsic SHE. The SHC was calculated via mapping DFT Hamiltonian to an effective Wannier Hamiltonian using Wannier90 approach and by

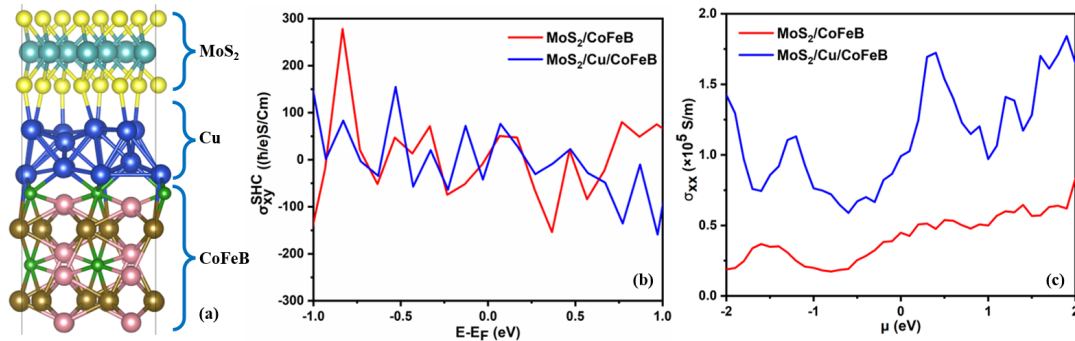


FIG. 4. (a) Structural model for the MoS<sub>2</sub>/Cu/CoFeB considered for the DFT-Wannier calculations for the spin transport. (b) Spin Berry conductivity as a function of energy relative to the Fermi energy, (c) the longitudinal charge conductivity as a function of the chemical potential.

using Kubo's formula given by [36, 37],

$$\sigma_{xy}^{SHC}(E) = -\frac{e^2}{\hbar} \frac{1}{VN} \sum_{nk} \Omega_{nk,xy}^{\text{spin},z}(E) f_{nk} \quad (8)$$

Here summation over  $n$  is performed over all occupied bands, and  $N$  is the number of  $k$ -points in the first Brillouin zone.  $f_{nk}$  is the Fermi-Dirac distribution function. The spin Berry curvature is defined by [36, 37],

$$\Omega_{nk,xy}^{\text{spin},z}(E) = \hbar^2 \sum_{m \neq n} \frac{-2 \text{Im} \left[ \langle \psi_{nk} | \frac{2}{\hbar} \hat{j}_x | \psi_{mk} \rangle \langle \psi_{mk} | \hat{v}_y | \psi_{nk} \rangle \right]}{(\epsilon_{nk} - \epsilon_{mk})^2 - (E + i\eta)^2} \quad (9)$$

The longitudinal charge conductivity was calculated using the BOLTZWANN module [38].  $\hat{j}_x^s$  is the spin-current operator given by  $\hat{j}_x^s = \frac{1}{2} \{ \hat{s}_z, \hat{v}_x \}$

The calculated SHA ( $\theta_{\text{SHA}}$ ) for the MoS<sub>2</sub>/CoFeB is 0.022 while for MoS<sub>2</sub>/Cu/CoFeB the corresponding value is 0.043. This supports the experimental claim that Cu effectively decouples MoS<sub>2</sub> from the magnetic exchange interaction with CoFeB, preserving the spin-orbit coupling (SOC) properties of MoS<sub>2</sub>. Our theoretical results further validate the assertion that the intrinsic SHE, a key mechanism for spin-charge conversion in such systems, is augmented by interfacial modifications.

In Fig.4(a) we show the atomic structure of the MoS<sub>2</sub>/Cu/CoFeB heterostructure under consideration, while in the Fig.4 (b) we plot the spin Hall conductivity ( $\sigma_{xy}^{\text{SHC}}$ ) as a function of energy relative to the Fermi energy ( $E - E_F$ ) for the two configurations. The red curve represents the MoS<sub>2</sub>/CoFeB system, while the blue curve corresponds to the MoS<sub>2</sub>/Cu/CoFeB system. Both curves exhibit oscillatory behavior, but the blue curve shows more periodic peaks than the red curve. In Fig.4 (c) we show the longitudinal charge conductivity ( $\sigma_{xx}$ ) is plotted as a function of the chemical potential ( $\mu$ ) for the two configurations.

From the denominator of Eq. 9, it is evident that peaks in the spin Hall conductivity (Fig. 4(b)) are associated

with avoided crossings in the band structure near the Fermi level, which directly influence the spin Berry curvature due to spin-orbit coupling (SOC) effects. In the MoS<sub>2</sub>/CoFeB system, proximity-induced exchange interactions at the interface modify the electronic structure of MoS<sub>2</sub>, partially suppressing its intrinsic SOC. The irregular peaks in the spin Hall conductivity suggest that the SOC effect is non-uniform and influenced by CoFeB's magnetic properties. Introducing a Cu interlayer between MoS<sub>2</sub> and CoFeB decouples MoS<sub>2</sub> from these magnetic interactions, resulting in more symmetric peaks in the spin Berry curvature for the MoS<sub>2</sub>/Cu/CoFeB system. This results in enhanced spin Hall conductivity and reduced interfacial scattering in the Cu-intercalated system. This can be further understood by our calculation of magnetic anisotropy energy (MAE). Indeed, our calculated MAE values strongly support the discussion of spin Berry curvature and spin Hall conductivity behavior. The higher MAE for the MoS<sub>2</sub>/Cu/CoFeB ( $9.83 \times 10^6$  erg/cm<sup>3</sup>) system compared to MoS<sub>2</sub>/CoFeB ( $7.2 \times 10^6$  erg/cm<sup>3</sup>) aligns well with the enhanced preservation of SOC and reduced proximity-induced effects in the Cu-intercalated structure. This increased anisotropy reflects the effectiveness of the Cu-interlayer in decoupling MoS<sub>2</sub> from CoFeB, allowing MoS<sub>2</sub>'s intrinsic properties to dominate. Such consistency between MAE calculations and spin transport properties further ensures the importance of interface engineering for optimizing spintronic device performance.

## CONCLUSION

We demonstrated a significantly enhanced spin-to-charge conversion efficiency, increased by an order of magnitude, through Cu intercalation in the MoS<sub>2</sub>/CoFeB system. Domain imaging revealed that Cu effectively decouples MoS<sub>2</sub> from proximity effects with CoFeB. These experimental results are further supported by theoretical calculations using the DFT-WANNIER90 framework,

which show notable improvements in spin Berry curvature, spin Hall conductivity, and magnetic anisotropy energy. Using the first-principles based calculations, we demonstrate that Cu intercalation preserves the intrinsic SOC of MoS<sub>2</sub> by decoupling it from CoFeB's magnetic exchange interactions, leading to a significant enhancement in the spin Hall effect. Our findings may pave the way for the development of highly efficient spintronic devices by leveraging intercalation strategies to engineer material interfaces.

## ACKNOWLEDGMENTS

AM, RC, SD, SS, KSR, and S. Bedanta thank the Department of Atomic Energy (DAE), Government of India, for the financial support via project with Sanct. No. 0803/2/2020/NISER/R&D-II/8149 dated 16.07.2021). The authors acknowledge SERB project (CRG/2021/001245 dated 05.03.2022) for financial assistance.

---

\* [s.bhattacharjee@ikst.res.in](mailto:s.bhattacharjee@ikst.res.in)

† [sbedanta@niser.ac.in](mailto:sbedanta@niser.ac.in)

- [1] A. Hirohata, K. Yamada, Y. Nakatani, I.-L. Prejbeanu, B. Diény, P. Pirro, and B. Hillebrands, *Journal of Magnetism and Magnetic Materials* **509**, 166711 (2020).
- [2] A. Soumyanarayanan, N. Reyren, A. Fert, and C. Panagopoulos, *Nature* **539**, 509 (2016).
- [3] J. Ryu, S. Lee, K.-J. Lee, and B.-G. Park, *Advanced Materials* **32**, 1907148 (2020).
- [4] Y. Tserkovnyak, A. Brataas, and G. E. Bauer, *Physical Review B* **66**, 224403 (2002).
- [5] J. Hirsch, *Physical review letters* **83**, 1834 (1999).
- [6] E. Saitoh, M. Ueda, H. Miyajima, and G. Tatara, *Applied physics letters* **88** (2006).
- [7] K. Roy, A. Mishra, P. Gupta, S. Mohanty, B. B. Singh, and S. Bedanta, *Journal of Physics D: Applied Physics* **54**, 425001 (2021).
- [8] B. B. Singh, K. Roy, J. A. Chelvane, and S. Bedanta, *Physical Review B* **102**, 174444 (2020).
- [9] B. B. Singh and S. Bedanta, *Physical Review Applied* **13**, 044020 (2020).
- [10] M. Kimata, H. Chen, K. Kondou, S. Sugimoto, P. K. Muduli, M. Ikhlas, Y. Omori, T. Tomita, A. H. MacDonald, S. Nakatsuji, et al., *Nature* **565**, 627 (2019).
- [11] B. B. Singh, S. K. Jena, M. Samanta, K. Biswas, B. Satpati, and S. Bedanta, *physica status solidi (RRL)–Rapid Research Letters* **13**, 1800492 (2019).
- [12] M. Jamali, J. S. Lee, J. S. Jeong, F. Mahfouzi, Y. Lv, Z. Zhao, B. K. Nikolic, K. A. Mkhoyan, N. Samarth, and J.-P. Wang, *Nano letters* **15**, 7126 (2015).
- [13] J. F. Sierra, J. Fabian, R. K. Kawakami, S. Roche, and S. O. Valenzuela, *Nature Nanotechnology* **16**, 856 (2021).
- [14] Y. Liu, C. Zeng, J. Zhong, J. Ding, Z. M. Wang, and Z. Liu, *Nano-Micro Letters* **12**, 1 (2020).
- [15] V. P. Kumar and D. K. Panda, *ECS Journal of Solid State Science and Technology* **11**, 033012 (2022).
- [16] W. Choi, N. Choudhary, G. H. Han, J. Park, D. Akinwande, and Y. H. Lee, *Materials Today* **20**, 116 (2017).
- [17] D. Akinwande, N. Petrone, and J. Hone, *Nature communications* **5**, 5678 (2014).
- [18] Q. Xie, W. Lin, B. Yang, X. Shu, S. Chen, L. Liu, X. Yu, M. B. Breese, T. Zhou, M. Yang, et al., *Advanced Materials* **31**, 1900776 (2019).
- [19] V. Thiruvengadam, A. Mishra, S. Mohanty, and S. Bedanta, *ACS Applied Nano Materials* **5**, 10645 (2022).
- [20] A. Mishra, P. Gupta, V. Thiruvengadam, B. B. Singh, and S. Bedanta, *Journal of Alloys and Compounds* **970**, 172076 (2024).
- [21] J. Mendes, A. Aparecido-Ferreira, J. Holanda, A. Azevedo, and S. Rezende, *Applied Physics Letters* **112** (2018).
- [22] S. Husain, A. Kumar, P. Kumar, A. Kumar, V. Barwal, N. Behera, S. Choudhary, P. Svedlindh, and S. Chaudhary, *Physical Review B* **98**, 180404 (2018).
- [23] R. Bansal, A. Kumar, N. Chowdhury, N. Sisodia, A. Barvat, A. Dogra, P. Pal, and P. Muduli, *Journal of Magnetism and Magnetic Materials* **476**, 337 (2019).
- [24] C. Du, H. Wang, F. Yang, and P. C. Hammel, *Physical Review Applied* **1**, 044004 (2014).
- [25] E. Longo, L. Locatelli, M. Belli, M. Alia, A. Kumar, M. Longo, M. Fanciulli, and R. Mantovan, *Advanced Materials Interfaces* **8**, 2101244 (2021).
- [26] W. Zhang, M. B. Jungfleisch, W. Jiang, J. E. Pearson, and A. Hoffmann, *Journal of Applied Physics* **117** (2015).
- [27] S. Yakata, Y. Ando, T. Miyazaki, and S. Mizukami, *Japanese journal of applied physics* **45**, 3892 (2006).
- [28] A. Conca, B. Heinz, M. Schweizer, S. Keller, E. T. Papaioannou, and B. Hillebrands, *Physical Review B* **95**, 174426 (2017).
- [29] K. Ando, S. Takahashi, J. Ieda, Y. Kajiwara, H. Nakayama, T. Yoshino, K. Harii, Y. Fujikawa, M. Matsuo, S. Maekawa, et al., *Journal of applied physics* **109** (2011).
- [30] T. Zhou and D. Gall, *Physical Review B* **97**, 165406 (2018).
- [31] H. Wang, C. Du, Y. Pu, R. Adur, P. C. Hammel, and F. Yang, *Physical review letters* **112**, 197201 (2014).
- [32] Y. Xie, Q. Zhan, Y. Hu, X. Hu, X. Chi, C. Zhang, H. Yang, W. Xie, X. Zhu, J. Gao, et al., *NPG Asia Materials* **12**, 67 (2020).
- [33] P. Nayar and I. Batra, *Journal of magnetism and magnetic materials* **87**, 357 (1990).
- [34] N. Chowdhury and S. Bedanta, *AIP advances* **4** (2014).
- [35] D. Qu, S. Huang, B. Miao, S. Huang, and C. Chien, *Physical Review B* **89**, 140407 (2014).
- [36] G. Pizzi, V. Vitale, R. Arita, S. Blügel, F. Freimuth, G. Géranton, M. Gibertini, D. Gresch, C. Johnson, T. Koretsune, et al., *Journal of Physics: Condensed Matter* **32**, 165902 (2020).
- [37] J. Qiao, J. Zhou, Z. Yuan, and W. Zhao, *Physical Review B* **98**, 214402 (2018).
- [38] G. Pizzi, D. Volja, B. Kozinsky, M. Fornari, and N. Marzari, *Computer Physics Communications* **185**, 422 (2014).